APPLIED PHYSICS

Harnessing the topotactic transition in oxide heterostructures for fast and high-efficiency electrochromic applications

Ji Soo Lim[1,2], Jounghee Lee[1], Byeoung Ju Lee[3], Yong-Jin Kim[1,2], Heung-Sik Park[1,2], Jeonghun Suh[1,2], Ho-Hyun Nahm[4], Sang-Woo Kim[5], Byeong-Gwan Cho[5], Tae Yeong Koo[5], Eunjip Choi[3], Yong-Hyun Kim[1,4]*, Chan-Ho Yang[1,2,6]*

Mobile oxygen vacancies offer a substantial potential to broaden the range of optical functionalities of complex transition metal oxides due to their high mobility and the interplay with correlated electrons. Here, we report a large electro-absorptive optical variation induced by a topotactic transition via oxygen vacancy fluidic motion in calcium ferrite with large-scale uniformity. The coloration efficiency reaches ~80 cm^2 C^{-1}, which means that a 300-nm-thick layer blocks 99% of transmitted visible light by the electrical switching. By tracking the color propagation, oxygen vacancy mobility can be estimated to be 10^{-8} cm^2 s^{-1} V^{-1} near 300°C, which is a giant value attained due to the mosaic pseudomonoclinic film stabilized on $LaAlO_3$ substrate. First-principles calculations reveal that the defect density modulation associated with hole charge injection causes a prominent change in electron correlation, resulting in the light absorption modulation. Our findings will pave the pathway for practical topotactic electrochromic applications.

INTRODUCTION

Complex transition metal oxides have been extensively studied due to their intriguing physics and functionalities related to the interplay of the charge, spin, orbital, and lattice degrees of freedom (*1*, *2*). Recently, much attention has been paid to lattice defects such as oxygen vacancies and interstitials in these complex oxides (*3*–*8*). Significant control of their concentration by electrochemical redox reactions affects various physical properties, such as optical (*9*–*11*), magnetic (*12*), and electronic conduction characteristics (*13*), as well as crystalline and electronic structures (*14*). In particular, controlling ionized charged defects in an electric way provides a useful pathway into the emergence of exotic quantum phases that are hardly realized in thermodynamic equilibrium (*15*, *16*). Finding the controllability of those defects, along with examining competing electronic/defective states and related property modulation, is a promising research topic. In this context, it is very interesting but rarely explored to realize a prominent and high-speed change with large-scale uniformity in the optical contrast between two competing defective crystal structures beyond the conventional bandgap engineering. The conversion uses a topotactic transition, i.e., a structural change to a crystalline solid that is crystallographically equivalent to the original phase, which may include loss or gain of constituent elements (*17*–*19*). Because the large carrier injection is relatively difficult to achieve by conventional dopant substitution limited by the solubility, the electric field–induced topotactic transitions between (meta-)stable states in complex oxides offer a great opportunity for emergent functions.

Our model compound is calcium ferrite $CaFeO_{3-\delta}$ (CFO) that spontaneously contains a large number of oxygen vacancies ($\delta \sim 0.5$) to maintain the valence state of Fe^{3+} as a thermodynamically stable phase in ambient pressure. The oxygen vacancies are arranged in an ordered manner along a pseudocubic <110> axis, forming the brownmillerite structure of $CaFeO_{2.5}$ (*BM*-CFO) (*20*). It is an optically transparent and electronically insulating phase with an estimated bandgap of 2.5 eV (*21*). A topotactic transition by filling the vacancies with externally supplied oxygen anions can create another competing crystal structure that is the perovskite $CaFeO_3$ (*P*-CFO). Because an ionized oxygen vacancy plays the role of a double-electron donor, the transition induces a high valence state of Fe^{4+} and/or ligand hole. This stoichiometric phase can be emergent usually in extreme conditions through the application of a high pressure up to 3 GPa in air or of high-temperature annealing in an oxygen plasma environment (*22*, *23*). However, both ways are challenging to access device applications.

Here, we explore the possibility of a topotactic phase transition between the *BM*-CFO and *P*-CFO phases in epitaxial films through oxygen vacancy migration by the external electric fields as an alternative and readily accessible approach. The transparent *BM*-CFO is changed to a highly conducing dark-colored *P*-CFO. We quantify the optical absorption change in the visible range to be $\Delta\alpha = 2 \times 10^5$ cm^{-1} with a high coloration efficiency. The measured optical spectra are interpreted with first-principles density functional theory (DFT) calculation results, which propose that the hole carrier injection in oxygen-filled *P*-CFO reduces the effective on-site interaction on Fe 3d orbitals, giving a strong optical transition in the visible range in contrast to the relatively less probable O 2p to Fe 3d transition in the as-grown *BM*-CFO. The mobility of phase-boundary motion, attributed to collective oxygen vacancy electromigration, at an elevated temperature is approximately 10^{-8} cm^2 s^{-1} V^{-1}, indicating that a fast operation is feasible in the conventional geometry using a thin electrochromic layer. Furthermore, careful x-ray diffraction analyses not only clarify both of the competing crystal structures with

[1]Department of Physics, Korea Advanced Institute of Science and Technology (KAIST), Yuseong-gu, Daejeon 34141, Republic of Korea. [2]Center for Lattice Defectronics, KAIST, Yuseong-gu, Daejeon 34141, Republic of Korea. [3]Department of Physics, University of Seoul, Seoul 02504, Republic of Korea. [4]Graduate School of Nanoscience and Technology, KAIST, Yuseong-gu, Daejeon 34141, Republic of Korea. [5]Pohang Accelerator Laboratory, POSTECH, Pohang, Gyeongbuk 37673, Republic of Korea. [6]KAIST Institute for the NanoCentury, KAIST, Yuseong-gu, Daejeon 34141, Republic of Korea.
*Corresponding author. Email: chyang@kaist.ac.kr (C.-H.Y.); yong.hyun.kim@kaist.ac.kr (Y.-H.K.)

the epitaxial relationship with the substrate, which provides important clues of a strain relaxation mechanism for the fast ionic migration, but also confirm the occurrence of the charge disproportionation accompanied by the metal-insulator transition known to appear in the nearly stoichiometric phase. Our findings offer useful insights into a topotactic electrochromic material with high coloration efficiency, fast switching speed, and material durability.

RESULTS

Large-scale electrical forming process for the topotactic phase transition

The *BM*-CFO thin film spontaneously contains a lot of oxygen vacancies (16.7% oxygen ions are missing relative to the stoichiometric perovskite). Positively ionized oxygen vacancies can be migrated by electric fields, resulting in a nonuniform defect distribution with spatial separation of optical contrast. The oxygen-rich (oxygen vacancy poor) region is shown to be opaque due to the strong and broad absorption of photons in the visible light regime (Fig. 1A). We deposited an epitaxial *BM*-CFO thin film of 100-nm thickness on an $LaAlO_3$ (LAO) (001) substrate. The *BM*-CFO film was patterned to form a rectangular *BM*-CFO channel (400 μm long and 50 μm wide) between platinum coplanar electrodes to apply external electric fields. We post-deposited an optically transparent LAO film of 10 nm thickness on the entire area of the *BM*-CFO channel, including the substrate area and edges of the CFO channel, to maintain the electrically formed state for a long time. The capping layer assists to reduce the reaction between the channel and atmospheric environments because LAO has high oxygen vacancy formation energy of ~7.3 eV (*24*). Also, the LAO, used in the experiment, is optically stable under the application of external bias of 75 V.

To quantify the motion of oxygen vacancies, we analyze the real-time images of a long bar channel at 300°C during the electric field–driven defect flow process (Fig. 1B). As an external bias of 75 V is applied on this channel, dark spots appear unevenly near the positively biased electrode and spread out toward the negatively biased electrode. These dark areas expand and completely fill the channel except for a narrow area near the ground electrode. Considering that the area of the accumulated region is not sufficiently large enough to supply all oxygen ions to the formed channel, it can be deduced that a considerable portion of oxygen vacancies is moving out of the channel. During the electric field–driven defect flow, the conductivity rises to 10^3 higher than that of the *BM*-CFO and also shows an anomaly at the completion of the electroforming process (Fig. 1C). The time-dependent visualization also provides insights into the detailed evolution of color change during the oxygen vacancy migration. It exhibits the *BM*-CFO changes to the dark phase via an intermediate state (fig. S1A). The forming time is logarithmically proportional to the inverse of temperature due to the thermal activation process in ionic migration; however, the saturated electronic current after the forming exhibits little temperature dependence, suggesting that the dark-colored phase has a metallic electronic conduction. By considering the finite length of the channel of 400 μm, we obtain an average speed of oxygen vacancies as a function of temperature. We estimate ionic mobility (μ) using the relation, $\mu = v/E$, where v is the average speed and E is the average electric field (Fig. 1D). The activation energy barrier for oxygen vacancy migration records to be 0.75 eV, which is comparable to Ca 30% substituted $BiFeO_3$ thin films (*25*, *26*). In addition, the ionic mobility shows the order of

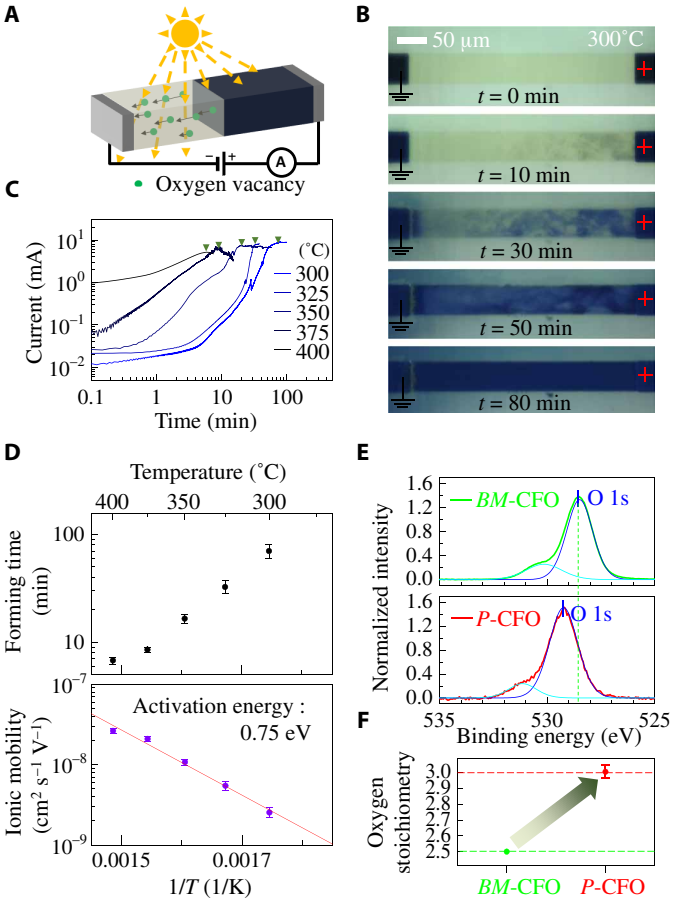

Fig. 1. Electrochromic process of a CFO thin film. (**A**) Schematic of an electrochromic CFO device. (**B**) Real-time optical images of a CFO channel during an electroforming process at a bias voltage of 75 V at selected elapsed times. (**C**) Real-time current monitoring during electroforming processes. Green marks indicate the forming time of each process. (**D**) Temperature dependences of the forming time and ionic mobility. Error bars were estimated to be one-fifth of the full-width half-maximum of the time derivative of the monitor current. (**E**) Oxygen 1s binding energy spectra of both *BM*-CFO and *P*-CFO, normalized by the integrated intensity of Ca 2p spectra. Each spectrum is deconvoluted into two (main and shoulder) peaks. (**F**) Oxygen stoichiometry of the formed state is estimated by comparing the spectral areas of the main peaks, on the assumption that the oxygen stoichiometry of *BM*-CFO is 2.5.

10^{-8} cm^2 s^{-1} V^{-1} between 300° and 400°C. We also investigated the voltage dependence of ionic migration. The higher forming voltage is applied, the more quickly the electroforming is completed. Even under the application of different external voltages, ionic mobility shows the similar order of magnitude (fig. S1). The ionic mobility we estimated using the collective migration and phase transition is distinct from the usual ionic mobility of a given material taken in the small perturbation regime. Intermediate phases between the two end phases and nonequilibrium states can be involved in the motion of defects.

Different oxygen contents on both states are investigated by using the O 1s binding energy spectra (Fig. 1E). Each spectrum is normalized by the peak area of Ca 2p binding energy spectrum of each state because Ca ions are not significantly affected by the forming process (fig. S2A). A 1-eV blue shift of the O 1s spectra indicates

that hole carriers appear in *P*-CFO and reduce screening charges in Fe—O bonding. Because *BM*-CFO has a charge-transfer insulating property, the Fermi level of *P*-CFO lies in the O 2p orbitals, which are hybridized to Fe orbitals, invoking the $Fe^{3+}\underline{L}$ ($\underline{L}$ denotes a ligand hole) rather than the Fe^{4+} state (fig. S2B) (*27*). In addition, we confirm 1-eV blue shift of the Fe 2p binding energy spectrum in *P*-CFO owing to the hole carriers in Fe—O hybridized orbitals. Each O 1s binding energy spectrum is split into two peaks. The main peaks (528 to 530 eV) originate from oxygen ions of the crystalline network, while the minor peaks are attributed to surface hydroxides or dangled oxygen ions at the surface. The spectral weight is proportional to the content of oxygen ions. By comparing the spectral areas of main peaks, we are led to the fact that the oxygen stoichiometry of *P*-CFO reaches "3," indicating that all oxygen vacancies are removed in *P*-CFO (Fig. 1F).

Electronic conduction and charge disproportionation

The stoichiometric *P*-CFO phase has been notoriously difficult to synthesize, and it has been limitedly successful in bulk materials annealed in high oxygen gas pressure (*22*). The ideal stoichiometric compound is known to exhibit a charge disproportionation as well as a metal-insulator transition (*23*). Therefore, we check whether the temperature-driven electronic phase transition occurs in the electrically formed area. As-grown *BM*-CFO film shows a highly insulating state of 10^4 ohm·cm at room temperature. On the other hand, the *P*-CFO phase is expected to have a high electronic conductivity due to the optically dark contrast after the electroforming process. The valence band also exhibits that *P*-CFO has finite states at the Fermi level, likely to show a metallic behavior (fig. S3). By using a set of measurement electrodes additionally deposited at the center of the *P*-CFO area (Fig. 2A), we confirmed that the *P*-CFO recorded a very low resistivity of 10^{-2} ohm·cm at room temperature. Such a large resistivity change by 10^6 suggests the generation of a huge amount of electronic free carriers in *P*-CFO, indicating that CFO is promising in terms of resistive switching as well as electrochromism. We found that a metal-insulator transition occurs at ~280 K in the electroformed film (Fig. 2B). Below the transition temperature, it is presumed that a charge-ordered gap brings the insulating state.

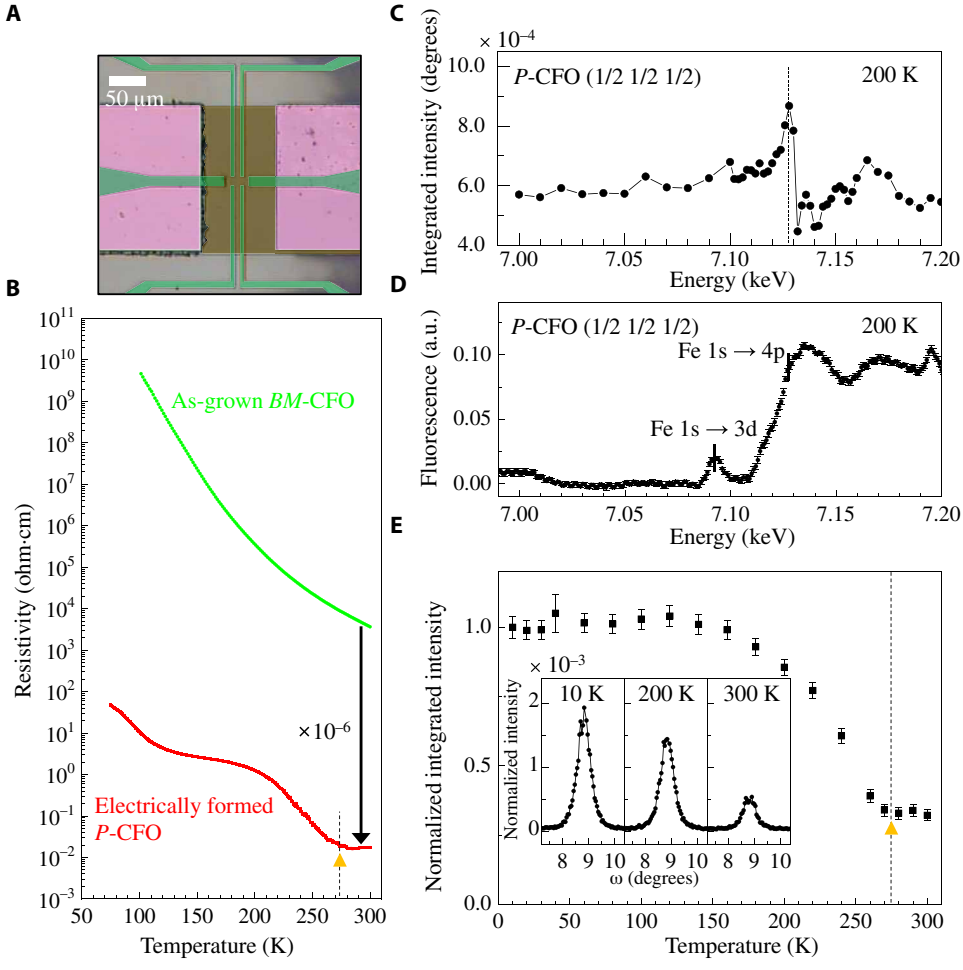

Fig. 2. Electronic conduction change and emergence of charge disproportionation. (**A**) Microscopic image of four-probe measurement electrodes (green) post-deposited on an electroformed *P*-CFO (dark yellow) between two forming electrodes (pink). (**B**) Electrical resistivity of *BM*-CFO and *P*-CFO. Dashed vertical line indicates a metal-insulator transition. (**C**) Energy-dependent integrated intensity of the (1/2 1/2 1/2) peak of *P*-CFO near Fe *K*-edge. The integrated intensity was obtained through areal integration of ω rocking curve. (**D**) Fluorescence near Fe *K*-edge at the (1/2 1/2 1/2) reflection. a.u., arbitrary unit. (**E**) Temperature-dependent integrated intensity of the (1/2 1/2 1/2) peak at 7.128 keV for *P*-CFO, rescaled by the value at the lowest temperature. The intensity was normalized by the integrated intensity of (0 1/2 2) at 7.128 keV. The inset graphs represent ω-rocking curves of (1/2 1/2 1/2) at 10, 200, and 300 K. Dashed line indicates the charge disproportionation transition.

To obtain direct evidence of the occurrence of charge disproportionation in the electrically formed area, we performed resonant x-ray scattering. We found that the pseudocubic (1/2 1/2 1/2) reflection of a *P*-CFO film has a resonant behavior associated with the charge disproportionation ($Fe^{3+}\underline{L} \rightarrow Fe^{3+} + Fe^{3+}\underline{L}^2$). The energy-dependent integrated intensity at 200 K shows a distinct peak enhancement at a photon energy of 7.128 keV (Fig. 2C). The resonance energy is consistent with the absorption edge of Fe 1s to 4p electric dipole transition observed in fluorescence (Fig. 2D), indicating that the 4p energy levels are influenced by the Fe charge state. The different Fe charge states induce distinct atomic form factors under the resonance condition, resulting in a pronounced diffraction peak at (1/2 1/2 1/2) in addition to the nonresonant background. A small peak at 7.09 keV in the pre-edge region is known to be due to the quadrupolar transition from Fe 1s to 3d (*28*). We examined the temperature dependence of the integrated intensity of the resonant peak at (1/2 1/2 1/2). The charge ordering emerges below 280 K, which coincides with the metal-insulator transition temperature (Fig. 2E).

Crystal structural analysis for a monoclinic to tetragonal transition with mosaicity

To gain hints on the reason why the topotactic transition is readily realized in CFO films on LAO substrate, we pay attention to a mosaicity associated with the crystal structure and strain relaxation by clarifying epitaxial relationship between the film and substrate. We performed x-ray diffraction on *BM*-CFO and *P*-CFO films to investigate the topotactic phase transition in terms of crystal structure, orientation, and mosaicity. The conventional θ-2θ scans show *c*-axis oriented films without detection of any impurity peaks (a full range scan is not shown here, Fig. 3A). The *P*-CFO phase has a notably smaller *c*-axis lattice parameter than *BM*-CFO due to the higher valence state of Fe^{4+} as a consequence of stronger Coulomb attraction between cations and anions.

The bulk crystal of *BM*-CFO has a distorted orthorhombic unit cell with space group *Pnma*, and a = 5.427 Å, b = 14.763 Å, and c = 5.597 Å (*29*), which is converted to the pseudocubic perovskite unit cell with c_p (a_p) $\approx \sqrt{a^2 + c^2}/2 = 3.898$ Å, and $b_p \approx b/4 = 3.691$ Å (Fig. 3B), where the pseudocubic c_p or a_p lattice parameters can deviate from 3.898 Å in opposite directions to form a rhombic cell ($\beta \neq 90°$). Oxygen vacancies in brownmillerites are periodically ordered along the $[100]_o$ direction (subscript "o" denotes the orthorhombic index). In the following, we will show that *BM*-CFO thin films grown on (001) LAO substrate have the orthorhombic *c*-*a* plane to be perpendicular to the substrate, more specifically, $[100]_o \parallel [101]_{sub}$, $[010]_o \parallel [010]_{sub}$, and $[001]_o \parallel [\bar{1}01]_{sub}$. In addition, the two in-plane axes of LAO (100) are equivalent to each other, so it is natural to consider the four-variant twin structure.

The alternating appearance of an octahedron layer and a tetrahedron layer along $[010]_o$ ($\parallel [010]_{sub}$ or $[100]_{sub}$) produces superlattices at [0 ±1/2 0] or [±1/2 0 0] around the (002) peak (Fig. 3C). Two additional satellite peaks close to the central peak are observed, which are more clearly detected in the reciprocal space map for (002) reflection (Fig. 3D). The symmetric peak splits in the (001), (002), and (004) reflections on the same line slanted 1.24° proving a mosaic rotation angle (fig. S4, A and B). To get information of in-plane axes, we carried out reciprocal space map around the (103) peak (Fig. 3E). The measured peak splitting can be interpreted based on the pseudomonoclinic unit cell compatible with the bulk orthorhombic phase and the mosaic rotation. The monoclinic angle related to the *L*-splitting of (103) and ($\bar{1}$03) peaks is determined to be $\beta = 88.76° = 90° - 1.24°$, which is equivalent to the mosaic rotation angle, and as a result, the monoclinic *c* axis becomes perfectly normal to substrate (Fig. 3E and fig. S4C). The *BM*-CFO film has a four-variant twin structure consisting of $a^{\pm}(b^{\pm})$-twins tilted by ±1.24° around the $a(b)$ axis, which is reminiscent of the ferroelastic WO_3 crystal structure (*30*). The larger peak intensity at (1.031, 2.928) [reciprocal lattice unit (r.l.u.)] is due to superposition of three reflections, +1.24°-rotated ($\bar{1}$03), (013), and (0$\bar{1}$3), while the −1.24°-rotated (103) reflection appears as a weak peak at a rather small *H* position. The original *H* position (0.968 r.l.u.) of (103) and ($\bar{1}$03) peaks and that (1.031 r.l.u.) of (013) and (0$\bar{1}$3) are separated at equal intervals from that of LAO substrate. Provided that $a^{\pm}$ and $b^{\pm}$-twins are equally distributed, the interfacial energy due to misfit strain can be minimized.

On the other hand, the *P*-CFO film has a noticeable reduction of the oxygen vacancy superlattice peaks (Fig. 3F). From the reciprocal space maps, we confirm that the *P*-CFO film is described by a pseudotetragonal unit cell that is fully strained on LAO substrate (Fig. 3, G and H). When an external electric field removes oxygen vacancies, the mosaic crystal structure of the *BM*-CFO was rearranged to be a single tetragonal structure in *P*-CFO with a contracted pseudocubic *c*-axis lattice parameter (Fig. 3I). The interfacial contact area does not change during the topotactic transition into the fully strained phase. It might be a necessary requirement for minimizing the interfacial energy and improving the functionality and material endurance.

The role of mosaicity for fast ionic migration and comparison with cases on other substrates

The prominently high ionic mobility measured in this CFO film on LAO is related to the peculiar interfacial strain relaxation through the monoclinic twin structure without a large deformation of the bulk phase. The four-variant monoclinic twin structure is revealed as a mosaic surface topography with nanodomains of ~50-nm size (Fig. 4A). These nanodomains are spread over the entire area of the *BM*-CFO film. The edges of nanodomains are mostly parallel to [010] or [100] of LAO substrate. Because the unit cell of the monoclinic *BM*-CFO phase has different in-plane lattice parameters of a_p and b_p, which are larger or smaller than those of substrate, the twin structure of the alternating *a*- or *b*-domain array (a type of ferroelastic domains) efficiently relieves the misfit strain. The domain boundaries between differently oriented nanodomains are expected to have large strain gradients and lattice imperfections, which provide an efficient pathway of ionic migration, in a similar context to grain boundaries in Yttria-stabilized zirconia (YSZ) ionic conductor (*31*).

On the basis of the nonuniform dark contrast at the initial stage of forming (Fig. 1B) and the two-step process with emergence of an intermediate-state region (fig. S1A), as well as consideration of the mosaic domain pattern, we propose a hypothetical scenario for the ionic migration in this sample. As illustrated in Fig. 4B, oxygen vacancies within the domain boundaries are more rapidly migrated by electric fields, appearing an irregular vague dark phase in the middle of topotactic transition. After the oxygen vacancy density within domain boundaries is reduced, remnant oxygen vacancies in domains are coming out to completely transform to the dark phase (*P*-CFO). From the comparison experiments with other films on different substrates below, it is clear that the mosaicity and granular feature are critical for fast ionic migration in this compound. Grain

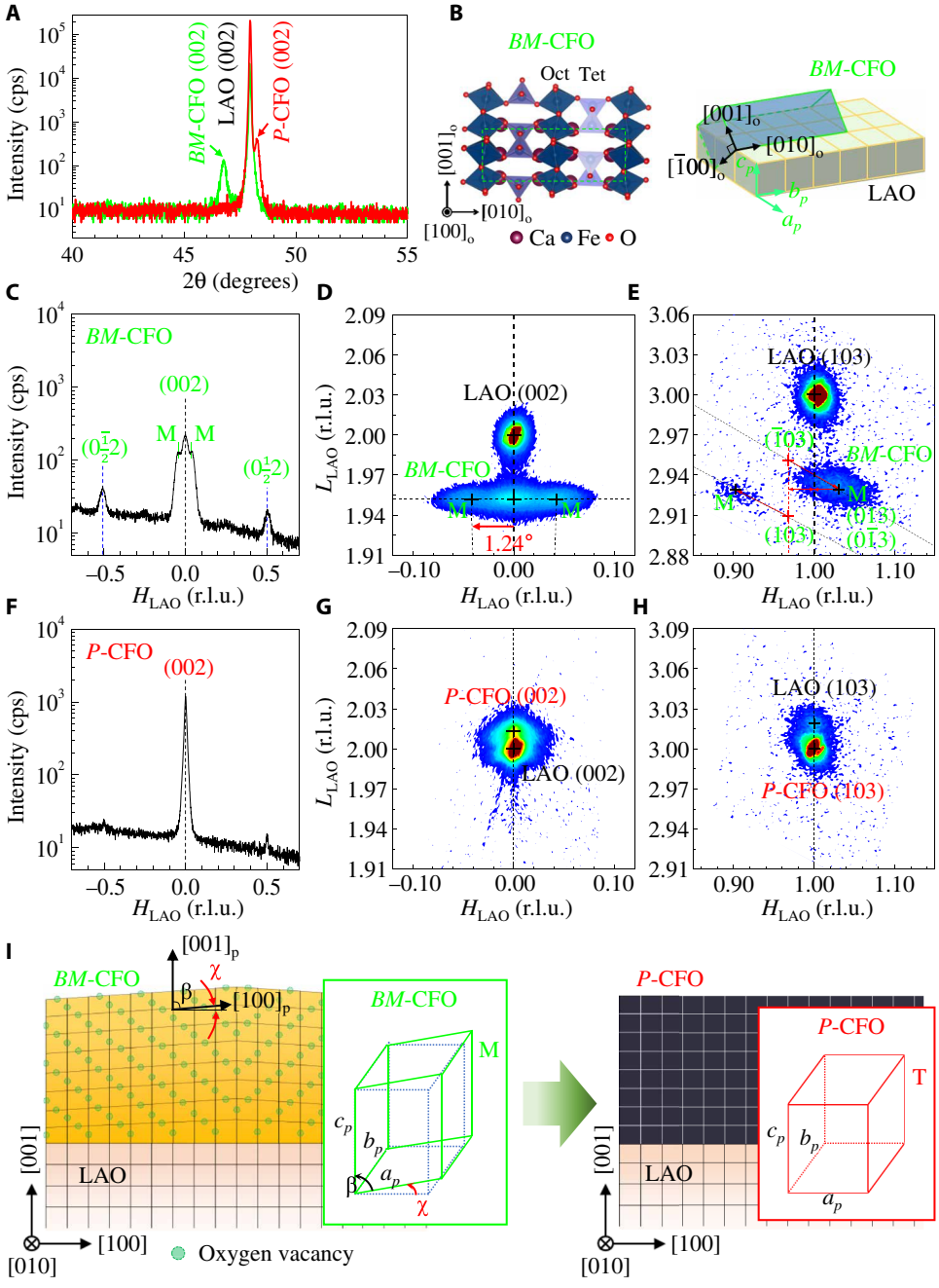

Fig. 3. Transformation of crystal structure in electroforming process. (**A**) X-ray θ-2θ scans for *BM*-CFO and *P*-CFO films on LAO substrate. (**B**) Orthorhombic unit cell of *BM*-CFO phase and the relationship with the pseudocubic unit cells of a film on LAO substrate. (**C**) Reciprocal line scan along an in-plane *H* direction at the *BM*-CFO (002) position. The reciprocal lattice unit (r.l.u.) is normalized by that of LAO. (**D**) Reciprocal space maps for (002) and (**E**) (103) reflections of a *BM*-CFO thin film. (**F**) Reciprocal line scan along the *H* direction at the *P*-CFO (002) position. (**G**) Reciprocal space maps for (002) and (**H**) (103) reflections of a *P*-CFO thin film. (**I**) Schematic of the oxygen vacancy arrangements for mosaic *BM*-CFO domains with pseudomonoclinic (M) cells. Pseudocubic lattice constants of the *BM*-CFO are measured to be $a_p = 3.914$ Å, $b_p = 3.675$ Å, $c_p = 3.883$ Å, $\alpha = \gamma = 90°$, and $\beta = 88.76°$. The transformed tetragonal (T) *P*-CFO phase has lattice constants of $a_p = b_p = 3.789$ Å, $c_p = 3.768$ Å, $\alpha = \beta = \gamma = 90°$.

boundaries can provide efficient routes for the migration of defects. As if a network of blood vessels carries and transports oxygen to individual living cells, both rapid movement through grain boundaries and interdiffusion between grains and grain boundaries occur cooperatively.

We perform an electroforming process on *BM*-CFO films grown on various substrates [$SrTiO_3$ (STO), $(La_{0.3}Sr_{0.7})(Al_{0.65}Ta_{0.35})O_3$ (LSAT), and $LaSrAlO_4$ (LSAO)] to clarify the importance of nanodomain formation in strain relaxed monoclinic films. All *BM*-CFOs on these substrates show atomically flat surfaces with step terraces (Fig. 4C). They have been reported to have tetragonal structures, epitaxially strained on their substrates (*29*). We fabricated long-bar channels (400 μm long and 50 μm wide) with 10-nm LAO capping layer, which have the same geometry of the *BM*-CFO film on LAO

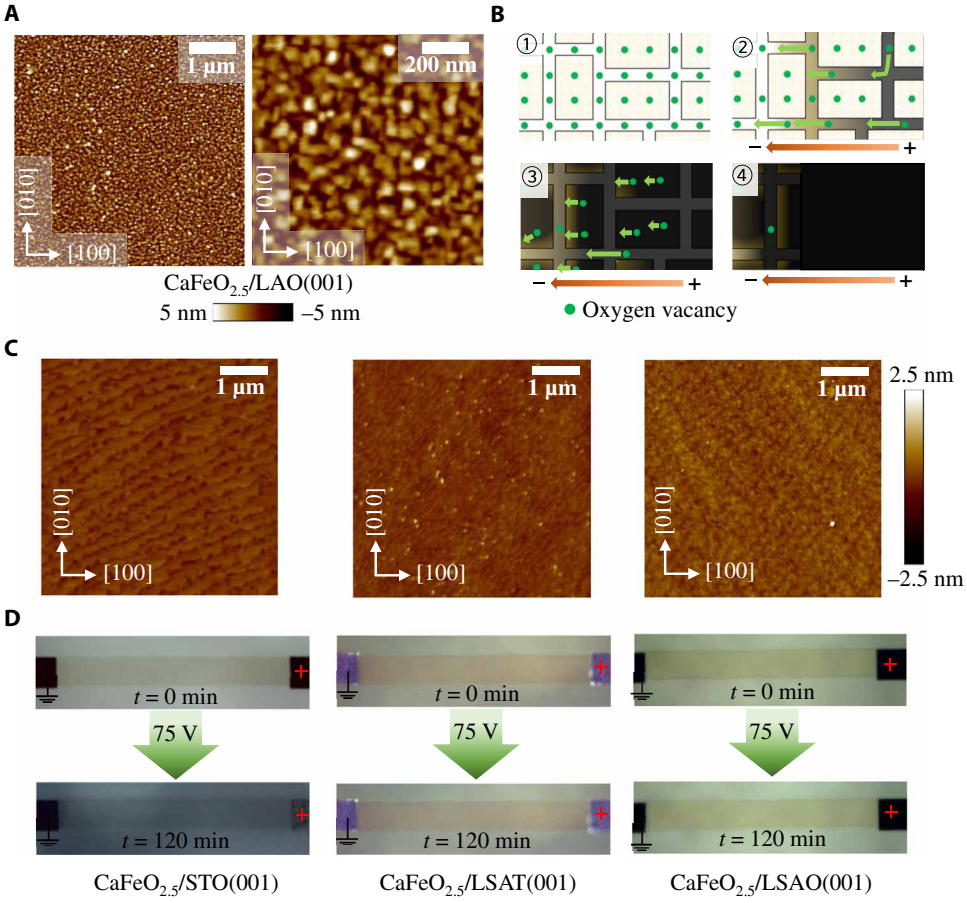

Fig. 4. Electroforming effects on *BM*-CFO films on various substrates. (**A**) The surface topography of a 100-nm-thick *BM*-CFO film on LAO shows nanodomains of ~50 nm in lateral size. The surface roughness (SD of surface height) is evaluated to be 1.62 nm. (**B**) Schematics of hypothetical oxygen vacancy migration steps through the mosaic structure. The yellow dotted boxes represent mosaic domains, and the domain walls appear between the domains. Oxygen vacancies (green balls) rapidly move through the wall regions, and they are also supplied from the domain regions through relatively slow diffusion. (**C**) Surface topographic images of as-grown *BM*-CFO films on various substrates [from left to right, STO(001), LSAT(001), and LSAO(001)]. (**D**) Initial (t = 0 min) and final (t = 120 min) microscopic still images of *BM*-CFOs during the electroforming processes.

substrate. When an external bias of 75 V was applied at 300°C for 2 hours on these *BM*-CFOs, none of them showed notable film color changes. In case of *BM*-CFO on STO(001) substrate, the external bias rather makes the STO substrate become darker, reminiscent of color change and blue light emission associated with oxygen vacancy creation (*32*, *33*). Even if the STO is influenced by the external bias, its *BM*-CFO does not show a distinct color change. Oxygen vacancies in tetragonal *BM*-CFOs fully strained to substrates are much stable and thus hard to migrate, indicating that the structurally relaxed films with mosaic nanodomain formation are a key factor for high-speed switching.

We also performed the backward forming by controlling the polarity of electric bias. The electroformed *P*-CFO can be returned to *BM*-CFO via an intermediate phase (gray-yellow region) by applying an external bias to the opposite direction (fig. S5, A and B). The gray-yellow phase is presumed to have less oxygen vacancies than the pristine *P*-CFO. In the initial forward forming process, the total amount of oxygen vacancies seems to be not perfectly conserved within the channel between the coplanar electrodes. The highly confined oxygen vacancies in the accumulative region can more easily diffuse into surrounding materials such as the LAO substrate, the capping layer, and the extra channel of CFO material extended underneath Pt electrode. A thorough understanding of the redox reaction in the vicinity of the ground electrode still remains a challenge. In addition, the *P*-CFO region can repeatedly expand and contract according to the direction of external bias alternately changed (fig. S5, C and D). The formed phase can return to *BM*-CFO by thermal annealing at 300°C for 4 hours. We confirmed that the crystal structure of the thermally relaxed *BM*-CFO was the same as that of the original *BM*-CFO (fig. S6). The sufficient annealing time for the recovery depends on the thickness of the capping layer as well as temperature because oxygen ions should be ejected to the environment through the capping layer. The stability at low temperatures (<400°C) can promote the functionality and lifetime of future devices.

Optical absorption property and coloration efficiency

To investigate the electrochromic effect on *P*-CFO, we carried out measurements of dielectric constants on both films, *BM*-CFO and *P*-CFO, by using variable angle ellipsometry. Optical ellipsometry provides an optical complex function, $\varepsilon = \varepsilon_1 + i\varepsilon_2$, without a Kramers-Krönig transformation and reference measurement. The imaginary part of dielectric constant ε_2 indicates an absorption loss that

characterizes the electronic band structure. In Fig. 5A, ε_1 and ε_2 of the *BM*-CFO demonstrate three main band excitations. Two main peaks at 3.2 eV (β_E) and 4.2 eV (γ_E) are most likely assigned to charge-transfer transitions from O 2p to Fe 3d band, but a more rigorous discussion will be undertaken based on first-principles calculations in the following section. Regardless of the existence of a defect level, ε_2 is quite small at low energies. Meanwhile, the ε_2 spectrum of *P*-CFO shows a broad peak around 2.3 eV (ζ_E), which is attributed to the optical transition from the O 2p to Fe 3d band (Fig. 5B). A Drude-like upturn is found to the extent that ε_2 is more than 10 in the infrared region, which seems to accord with the metallic behavior. A more detailed study of optical conductivity in the lower energy regime exhibits a gap-like characteristic (below 0.6 eV) that changes commensurately with the charge disproportionation when temperature is lowered (fig. S7).

The absorption coefficient (α) and extinction coefficient ($\tilde{k}$) can be calculated using the equations, $\alpha = 2\omega\tilde{k}/c$ and $\tilde{k}^2 = ((\varepsilon_1{}^2 + \varepsilon_2{}^2)^{1/2} - \varepsilon_1)/2$, where ω is photon frequency and c is the speed of light. The α value of the *P*-CFO is recorded to be 1.9×10^5 to 3.5×10^5 cm^{-1} in the visible light region (Fig. 5C). That is a large value compared to other $3d^4$ oxide systems, such as $LaMnO_3$ and $NdMnO_3$ (*34*). Meanwhile, *BM*-CFO shows an abrupt drop of α below 3 eV. Its optical bandgap is estimated to have a similar value of $BiFeO_3$ of 2.67 eV (*35*), and a midgap peak at 1.8 eV is thought to arise from defect states (*9*) such as imperfection of oxygen vacancy ordering. The two topotactically switchable phases provide an ideal electrochromic effect in the range of visible light (as guided by two dashed vertical lines). From the large modulation of the absorption coefficient ($\Delta\alpha$) as much as ~1.5×10^5 cm^{-1}, we infer that a *P*-CFO film of 300 nm thickness can screen 99% of light illumination (Fig. 5D). Under a conservative assumption that all the hole carriers induced by the full oxidation contribute to the optical absorption change, the modulated charge density is calculated to be ~2900 C cm^{-3} [e/(unit cell volume)], and thus, coloration efficiency (defined as absorption coefficient change normalized by charge density modulation) can be estimated to be more than 30 cm^2 C^{-1} in the visible light region and reaches the maximum of 80 cm^2 C^{-1} at a blue color, which is comparable to a value reported in a conventional electrochromic oxide, WO_3 (*36*).

Optical properties from the first-principles calculation

We performed first-principles DFT calculations to precisely understand the electronic structures and optical properties of *BM*-CFO and *P*-CFO for electrochromism. We first analyzed electronic structure, i.e., the site- and orbital-decomposed density of states (DOS) and band structure of *BM*-CFO and *P*-CFO, as shown in Fig. 6 and fig. S8. The *BM*-CFO is an antiferromagnetic (AFM) insulator with a bandgap of 2.2 eV, which is composed of a valence band dominated by the O 2p state and a conduction band dominated by the Fe 3d state (Fig. 6A). The Fe 3d bands in the tetrahedron are more localized because of the disconnected Fe—O bonding. The O 2p band shows a more dispersed band due to the connected Fe—O bonding

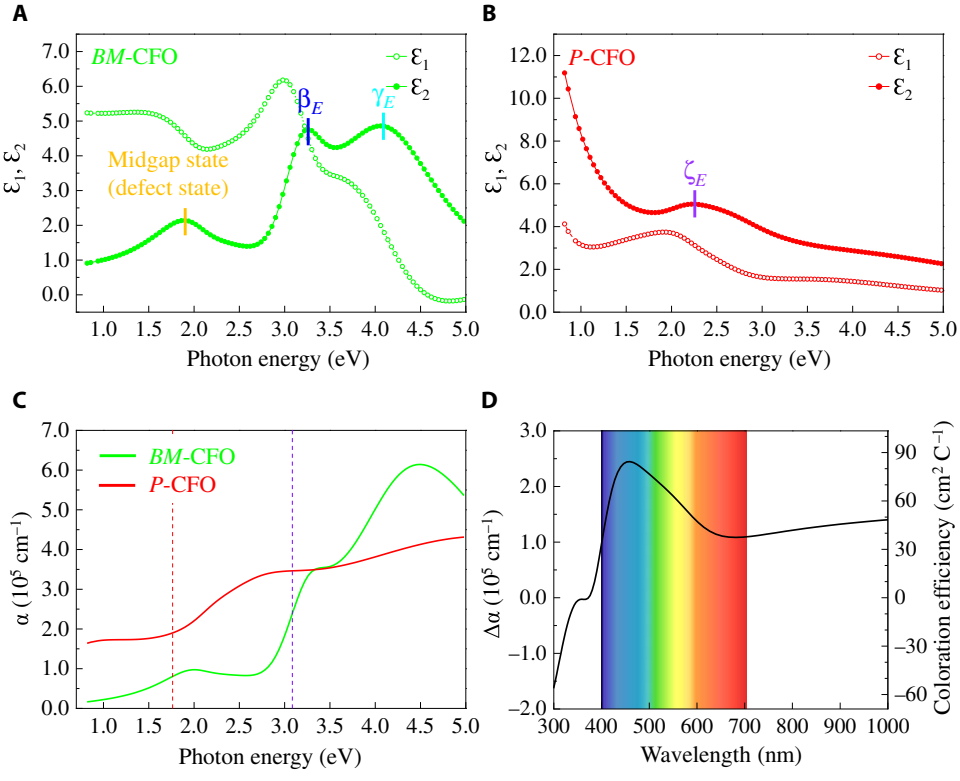

Fig. 5. The measured dielectric function and absorption coefficient spectra of CFO thin films on LAO substrate. (**A**) Real and imaginary dielectric function spectra of *BM*-CFO phase. The two main peaks at 3.2 eV (β_E) and 4.2 eV (γ_E) in the imaginary part are attributed to O 2p to Fe 3d optical transition. The relatively weak peak at 1.8 eV is likely caused by defect states. (**B**) Real and imaginary dielectric function spectra of *P*-CFO phase. The broad peak at 2.3 eV (ζ_E) is due to the interband O 2p to Fe 3d transition. (**C**) Absorption coefficient spectra of *BM*-CFO and *P*-CFO phases, calculated from the dielectric functions. Two vertical dashed lines guide the visible light region. (**D**) Absorption coefficient change and coloration efficiency for the topotactic transition from *BM*-CFO to *P*-CFO.

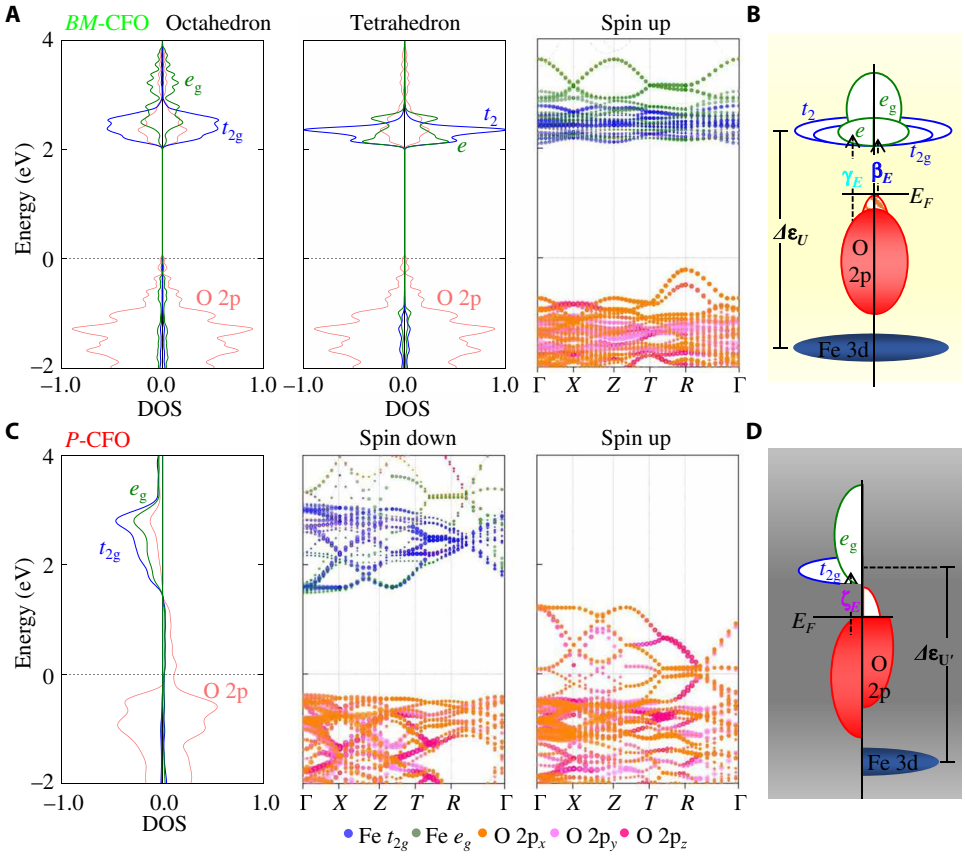

Fig. 6. Calculated electronic structure of *BM*-CFO and *P*-CFO. (**A**) Site- and orbital-decomposed DOS and band structure of AFM *BM*-CFO. (**B**) Schematic electronic structure of *BM*-CFO. β_E and γ_E indicate the optical transitions in its imaginary part of dielectric function spectra. (**C**) Site- and orbital-decomposed DOS and band structure of *P*-CFO. (**D**) Schematic electronic structure of *P*-CFO. ζ_E represents the optical transition in its imaginary part of dielectric function spectra.

in the [101] direction of the octahedron. The schematic band diagram of *BM*-CFO in Fig. 6B shows that the optical transition from the considerably (slightly) dispersed O 2p bands to unoccupied Fe 3d bands is the origin of the "β_E" ("γ_E") peak.

On the other hand, the *P*-CFO at room temperature has been experimentally reported to have a *Pbnm* structure, paramagnetic (PM), and metallic characteristics (*23*). We used noncollinear magnetic sampling methods (*37*) to consider the PM property of randomly arranged spin configuration in *P*-CFO. The total DOS in PM ordering is found to be qualitatively similar to total DOS (spin-up + spin-down) in a ferromagnetic (FM) region (fig. S9). Therefore, we analyzed the electronic structure of FM *P*-CFO, instead of computationally cumbersome PM *P*-CFO. The dispersion of O 2p related bands is further enhanced in the *P*-CFO than in the *BM*-CFO because the oxygen ions occupied at the oxygen vacancy sites connect each Fe—O bond to form three-dimensional octahedral channels (Fig. 6C). Moreover, the O 2p band is partially filled (metallic) in the spin-up direction, but the bandgap of 1.8 eV appears between the occupied O 2p band and unoccupied Fe 3d in the spin-down direction. Figure 6D shows a schematic of optical transitions in *P*-CFO. While the Drude-like peak at low photon energy originates from the spin-up optical transitions between the occupied and unoccupied O 2p bands, a broad peak in the visible light region, denoted by "ζ_E," can theoretically be described by the spin-down optical transition from the O 2p in the slightly dispersive valence band to the Fe 3d band in the considerably dispersive conduction band. This indicates that the difference between the β_E transition of the *BM*-CFO and the ζ_E transition of the *P*-CFO is a major cause of high coloration in the visible light region.

To verify the above analysis of the optical absorption variation, we calculated the dielectric constants and optical absorptions for both *BM*-CFO and *P*-CFO. The calculated imaginary parts and optical absorption coefficients of their dielectric constant are qualitatively similar to the experimental results (fig. S10, A and B). The peaks, assigned as β_E, γ_E, and ζ_E in the experimental data, are well reproduced from the calculated values. The calculated absorption coefficient is around 4×10^5 cm^{-1} in the visible light regime, which is the same order of magnitude of the experimental value (fig. S10C). The calculated coloration efficiency (fig. S10D) also reasonably agrees with the experimental data (Fig. 5D). Therefore, the rapid transparent-to-dark color change is explained by the modulation of optical properties due to the topotactic transition of *BM*-CFO to *P*-CFO.

DISCUSSION

It is remarkable that the absorption in the visible light regime in *P*-CFO reaches a high coloration efficiency of 80 cm^2 C^{-1}. On the basis of the above electronic structures of *BM*-CFO and *P*-CFO, we propose a possible scenario in which the modulation of effective on-site *U* energy of Fe causes the large change of the absorption coefficient.

Because O 2p bands in insulating *BM*-CFO and metallic *P*-CFO are fully and partially occupied, respectively, the effective on-site U and U' energies of Fe ions in *BM*-CFO and *P*-CFO are expected to be distinguished due to the different screening effects. This can be easily understood because the Hubbard-like on-site U energy on transition metal ion depends on ε_r ($U_{screen} \sim U_0/\varepsilon_r$), where U_0 is the on-site Coulomb interaction between electrons and ε_r is the relative permittivity. To check the validity of the assumption, we estimated the on-site U and U' to be 5.03 and 4.31 eV, respectively, in *BM*-CFO and *P*-CFO using the linear response approach (fig. S11) (*38*). Because U' is smaller than U, the spin-down energy splitting of $\Delta\varepsilon_{U'}$ between the O 2p bands and the Fe 3d bands in *P*-CFO is more reduced than of $\Delta\varepsilon_U$ in *BM*-CFO. The decrease in energy splitting from $\Delta\varepsilon_U$ to $\Delta\varepsilon_{U'}$ reduces the spin-down gap, where the interband transition starts from the O 2p bands to Fe 3d bands. This explains why the optical absorption in the visible energy region of the *P*-CFO can be very large.

To independently consider the difference in magnetic order and on-site U energy between the *BM*-CFO and the *P*-CFO, we individually estimated the contribution to the optical transitions of both the on-site U energy and spin configuration by comparing three types of *P*-CFO (FM metallic, AFM insulating, and FM insulating) in the same structure. This analysis shows that the low-energy optical transition of the spin-down channel in *P*-CFO is first caused by the on-site energy and followed by the spin configuration (fig. S12).

In conclusion, we found that oxygen vacancy migration in CFO induces an electrochromic effect with a large modulation of the absorption coefficient and the emergence of a metallic behavior. We carefully examined the topotactic phase transition between the brownmillerite and perovskite structures with observing the emergence and disappearance of the superlattice peaks associated with the oxygen vacancy ordering. We also experimentally confirmed that most of the oxygen vacancies were removed with a large-scale uniformity by the electrical forming process to the extent that the charge disproportionation transition is detected by the resonant x-ray scattering and the metal-insulator transition is also observed in the temperature-dependent electronic transport measurement. Moreover, we directly confirmed that the oxygen stoichiometry of the *P*-CFO approaches "3" by the comparative analysis of O 1s binding energy spectra. Furthermore, oxygen vacancies in the system were turned out to be highly mobile in electric fields, showing the large collective ionic mobility around 10^{-8} cm^2 s^{-1} V^{-1}. From these comprehensive and combined investigations of the theory and experiments, we can conclude not only that the CFO is a promising material for large electrocoloration effects but also that topotactic metallic transitions via ionic flows can be a key factor in designing fast and high-efficiency electrochromic devices through electron correlation control.

MATERIALS AND METHODS

Growth of epitaxial $CaFeO_{2.5}$ thin films

The epitaxial $CaFeO_{2.5}$ (CFO) thin films were grown on an LAO (001) substrate (CrysTec GmbH) using pulsed laser deposition equipped with a KrF excimer laser (λ = 248 nm). A pellet was prepared by mixing $CaCO_3$ (99.95%) and Fe_2O_3 (99.9%) powders (Sigma-Aldrich) and forming. The pellet was first heated at 850°C to eliminate CO_2 and then crushed, ground, and pressurized to make a 1-inch-diameter button-shaped target. It was calcined at 850°C for 8.5 hours at an ambient condition. After the calcination, the pellet proceeded with the same previous processes. Then, it was sintered at 900°C for 9 hours at an ambient condition. The epitaxial CFO thin films (~100 nm in thickness) were grown at a heater temperature of 650°C in an oxygen environment of 0.05 torr. Laser fluence and repetition rate were set to be ~1 J cm^{-2} and 10 Hz. All films were cooled down to room temperature at a rate of 10°C min^{-1} under an oxygen pressure of 500 torr.

Fabrication of BCFO microdevices and crystal structure characterization

Conventional ultraviolet (UV) lithography using a photoresist (AZ5214E, AZ Electronic Materials) was carried out to pattern a channel (400 μm long and 50 μm wide) on an as-grown CFO thin film. The patterned samples were dry-etched by the Ar^+-ion milling technique using a 2-cm-diameter ion beam source. During the etching process, the sample was continuously cooled by circulating cooling water to prohibit any thermal decomposition and degradation. We post-deposited an LAO capping layer (usually 10 nm in thickness, but a 20-nm-thick layer was used for the purpose of better protecting the highly confined oxygen vacancy region with a highly reactive redox tendency near the ground electrode for back-and-forth switching) on the entire sample surface including the substrate area and edges of the CFO regions by pulsed laser deposition to maintain the frozen state for a long time. The etched CFO film was put in the growth chamber again and heated to 650°C in an oxygen gas of 0.1 torr, and the epitaxial capping layer was deposited under the laser fluence and a repetition rate of ~1 J cm^{-2} and 2 Hz after the oxygen pressure is quickly dropped to 0.01 torr at the growth temperature. After the deposition, the sample was cooled down to room temperature at a rate of 10°C min^{-1} at an oxygen pressure of 500 torr. To produce the platinum electrodes required for the electrical contact with the external measurement equipment, their positions were patterned using the abovementioned UV lithography. The LAO capping layers on the patterned positions were removed by Ar^+ ion milling, and then platinum was in situ deposited by DC magnetron sputtering operated at an argon pressure of 5 mtorr with a power of 25 W at room temperature to contact the platinum electrodes directly on the surface of the CFO.

Electroforming process and crystal structure characterization

A high-voltage source (Tektronix, Keithley 237) and a multimeter (Tektronix, Keithley 2000) were used to perform the electroforming process on the CFO thin films. To prohibit film cracking during the electroforming process, current compliance was set to be 50 mA. The CFO film was mounted on a heating stage (Microptik, MHCS622-MTDC600). External voltage of 75 V was applied at high temperatures. The mobility was estimated as $\mu = v_{avr}/E_{avr} = L^2/(2t_{total}V)$. The average speed ($v_{avr}$) was defined as L/t_{total}, where L is the channel length and t_{total} is the total forming time, and the average electric field (E_{avr}) was defined as $2V/L$. Simultaneously, the electrical current and applied voltage were measured. The *c*-axis lattice parameters of the as-grown and electrically formed CFO thin films were measured using a four-circle x-ray diffractometer (PANalytical X'Pert PRO MRD) with Cu $K_{\alpha 1}$ radiation. We measured 2θ-ω x-ray scans from 10° to 60° with 1 s per point at an interval of 0.1°. We also performed reciprocal lattice maps at (002) and (103) reflections.

X-ray photoelectron spectroscopy of *BM*-CFO and *P*-CFO

We observed the binding energy spectra of each element of *BM*-CFO and *P*-CFO using x-ray photoelectron spectroscopy (Thermo Fisher Scientific, K-alpha). A focused x-ray beam (Al Kα, 1486.6 eV) with a diameter of 200 μm was injected onto the sample surface. The kinetic energy of the emitted photoelectrons was analyzed using a hemispheric analyzer with a 50-eV pass energy. The areas of consideration were etched by Ar ion milling (EX06 Ion Source) to remove the capping layer and surface contaminants. A low-energy electron flood gun was operated during the experiment to remove charging effects on both sample surfaces. Each binding energy spectrum was normalized by an intensity of Ca $2p_{3/2}$ because Ca was not much influential during the electroforming process. We used the Shirley method to extract the backgrounds of all the binding energy spectra. All spectra were analyzed using a commercial software (Thermo Fisher Scientific, Avantage 5923).

Resonant x-ray scattering

The resonant x-ray scattering was performed in the pressure of ~10^{-7} torr at the 3A beamline at Pohang Accelerator Laboratory. A Si(111) double-crystal monochromator was used to generate the incident light with σ-polarization, and the photon energy was calibrated using a Fe foil at its *K*-absorption edge (7.112 keV) within an energy resolution of 0.5 eV. The scattered light from the sample was detected via a highly oriented pyrolytic graphite (002) analyzer in a σ-π′ mode. The measured intensities were normalized by the monitor count of the incident x-ray beam.

Measurement of electronic conduction property

Electrical conductivity of *BM*-CFO was measured by the two-probe method using a high-resistance electrometer (Tektronix, Keithley 6517A). To investigate the electrical conductivity of *P*-CFO, we first patterned a coplanar channel (200 μm by 100 μm). The whole area of the *BM*-CFO region was encapsulated by the LAO capping layer of 2-nm thickness. After removing the capping layer on the electrode region, platinum was deposited at both sides of the channel to apply an external electric field. An external bias of 25 V was applied to transform the phase to *P*-CFO. After that, measurement electrodes were patterned at the center of the *P*-CFO region and etched to remove the capping layer, and last, platinum was deposited. The reason for using the exceptionally thin LAO layer of 2 nm thickness is to minimize a heating damage effect on the electroformed *P*-CFO during the LAO etching process, but it is sufficiently thick to protect the sample because the sample is mainly kept in low temperatures for the transport measurement. The electrical conductivity of *P*-CFO was measured by the four-probe method using a current source for applying a constant 5 μA (Tektronix, Keithley 6221) and a nanovoltmeter (Tektronix, Keithley 2182A) for measuring the voltage between the two central electrodes. Both of the films were characterized inside a Quantum Design Physical Property Measurement System (PPMS-9T) to control the temperature.

Optical absorption spectroscopy

We measured complex dielectric functions as a function of frequency in the range from near infrared to UV upon reflection, for both films *BM*-CFO and *P*-CFO, by using a variable angle ellipsometry (Woollam WVASE). The optical conductivity of *BM*-CFO and *P*-CFO on LAO was extracted from the dielectric functions as $\sigma_1(\omega) = \left(\frac{\varepsilon_2}{4\pi}\right)\omega$ (*39*).

Computational method

First-principles density functional theory calculations were carried out using the Perdew-Burke-Ernzerhof (PBE) exchange-correlation functional as implemented in the Vienna Ab-initio Simulation Package (VASP) (*40*). A cutoff energy of 500 eV was applied for the plane-wave basis set and a Γ-centered $4 \times 2 \times 4$ *k*-point mesh for the bulk $CaFeO_{2.5}$ and $8 \times 8 \times 8$ for the bulk $CaFeO_3$. The atomic positions were relaxed until the forces were less than 0.005 eV/Å, and the calculation result converged at the electronic energy of 10^{-5} eV. We applied a Hubbard-*U* correction of 5 eV to improve the description of the Fe 3d states in the *BM*-CFO and perovskites *P*-CFO. We found that the *BM*-CFO had orthorhombic lattice constants of 5.358, 15.156, and 5.649 Å and the *P*-CFO had cubic lattice constants of 7.641 Å, which are consistent with the experimental values.

The imaginary part of the dielectric function was obtained with the independent particle approximation in the long-wavelength limit $q \to 0$ by summation over the empty states using the following equation

$$\varepsilon^2_{\alpha\beta}(\omega) = \frac{4\pi^2 e^2}{\Omega} \lim_{q\to 0} \frac{1}{q^2} \sum_{v,c,\mathbf{k}} 2\,\omega_{\mathbf{k}}\,\delta(\varepsilon_{c,\mathbf{k}} - \varepsilon_{v,\mathbf{k}} - \omega) \langle u_{c,\mathbf{k}+e_{\alpha q}} \mid u_{v,\mathbf{k}} \rangle \langle u_{c,\mathbf{k}+e_{\beta q}} \mid u_{v,\mathbf{k}} \rangle^*$$

where the indices *v* and *c* refer to valence and conduction band states, respectively. $u_{n,\mathbf{k}}$ is the periodic part of the Bloch wave function (i.e., Kohn-Sham wave functions with the band index *n* are written as $\psi_{n\mathbf{k}}(\mathbf{r}) = u_{n,\mathbf{k}}(\mathbf{r})\, e^{i\mathbf{k}\cdot\mathbf{r}}$). $\omega_{\mathbf{k}}$ is the symmetry-associated weight factor and the factor "2" accounts for spin degeneracy. The $\mathbf{e}_\alpha$ or $\mathbf{e}_\beta$ are the unit vectors for the three Cartesian directions indication by α or β, and Ω represents the volume of the primitive cell. The real part, $\varepsilon^1_{\alpha\beta}(\omega)$ is generated via the Kramers-Krönig transformation.

SUPPLEMENTARY MATERIALS

Supplementary material for this article is available at http://advances.sciencemag.org/cgi/content/full/6/41/eabb8553/DC1

REFERENCES AND NOTES

1. D. Sando, Y. Yang, C. Paillard, B. Dkhil, L. Bellaiche, V. Nagarajan, Epitaxial ferroelectric oxide thin films for optical applications. *Appl. Phys. Rev.* **5**, 041108 (2018).
2. J. Varignon, M. Bibes, A. Zunger, Origin of band gaps in 3*d* perovskite oxides. *Nat. Commun.* **10**, 1658 (2019).
3. R. Gao, A. C. P. Jain, S. Pandya, Y. Dong, Y. Yuan, H. Zhou, L. R. Dedon, V. Thoréton, S. Saremi, R. Xu, A. Luo, T. Chen, V. Gopalan, E. Ertekin, J. Kilner, T. Ishihara, N. H. Perry, D. R. Trinkle, L. W. Martin, Designing optimal perovskite structure for high ionic conduction. *Adv. Mater.* **32**, 1905178 (2020).
4. N. Lu, P. Zhang, Q. Zhang, R. Qiao, Q. He, H.-B. Li, Y. Wang, J. Guo, D. Zhang, Z. Duan, Z. Li, M. Wang, S. Yang, M. Yan, E. Arenholz, S. Zhou, W. Yang, L. Gu, C.-W. Nan, J. Wu, Y. Tokura, P. Yu, Electric-field control of tri-state phase transformation with a selective dual-ion switch. *Nature* **546**, 124–128 (2017).
5. H.-X. Dong, J.-W. Luo, S.-H. Wei, Band structure engineering and defect control of oxides for energy applications. *Chin. Phys. B* **27**, 117104 (2018).
6. S. V. Kalinin, N. A. Spaldin, Functional ion defects in transition metal oxides. *Science* **341**, 858–859 (2013).
7. M. Campanini, R. Erni, C.-H. Yang, R. Ramesh, M. D. Rossell, Periodic giant polarization gradients in doped $BiFeO_3$ Thin Films. *Nano Lett.* **18**, 717–724 (2018).
8. S. J. Callori, S. Hu, J. Bertinshaw, Z. J. Yue, S. Danilkin, X. L. Wang, V. Nagarajan, F. Klose, J. Seidel, C. Ulrich, Strain-induced magnetic phase transition in $SrCoO_{3-\delta}$ thin films. *Phys. Rev. B* **91**, 140405 (2015).
9. J. Seidel, W. Luo, S. J. Suresha, P.-K. Nguyen, A. S. Lee, S.-Y. Kim, C.-H. Yang, S. J. Pennycook, S. T. Pantelides, J. F. Scott, R. Ramesh, Prominent electrochromism through vacancy-order melting in a complex oxide. *Nat. Commun.* **3**, 799 (2012).
10. K. K. Bharathi, W.-M. Lee, J. H. Sung, J. S. Lim, S. J. Kim, K. Chu, J. W. Park, J. H. Song, M.-H. Jo, C.-H. Yang, Detection of electrically formed photosensitive area in Ca-doped $BiFeO_3$ thin films. *Appl. Phys. Lett.* **102**, 012908 (2013).

11. W.-M. Lee, J. H. Sung, K. Chu, X. Moya, D. Lee, C.-J. Kim, N. D. Mathur, S.-W. Cheong, C.-H. Yang, M.-H. Jo, Spatially resolved photodetection in leaky ferroelectric $BiFeO_3$. *Adv. Mater.* **24**, OP49–OP53 (2012).
12. H. Jeen, W. S. Choi, M. D. Biegalski, C. M. Folkman, I.-C. Tung, D. D. Fong, J. W. Freeland, D. Shin, H. Ohta, M. F. Chisholm, H. N. Lee, Reversible redox reactions in an epitaxially stabilized $SrCoO_x$ oxygen sponge. *Nat. Mater.* **12**, 1057–1063 (2013).
13. C.-H. Yang, J. Seidel, S. Y. Kim, P. B. Rossen, P. Yu, M. Gajek, Y. H. Chu, L. W. Martin, M. B. Holcomb, Q. He, P. Maksymovych, N. Balke, S. V. Kalinin, A. P. Baddorf, S. R. Basu, M. L. Scullin, R. Ramesh, Electric modulation of conduction in multiferroic Ca-doped $BiFeO_3$ films. *Nat. Mater.* **8**, 485–493 (2009).
14. Q. Zhang, X. He, J. Shi, N. Lu, H. Li, Q. Yu, Z. Zhang, L.-Q. Chen, B. Morris, Q. Xu, P. Yu, L. Gu, K. Jin, C.-W. Nan, Atomic-resolution imaging of electrically induced oxygen vacancy migration and phase transformation in $SrCoO_{2.5-\sigma}$. *Nat. Commun.* **8**, 104 (2017).
15. J. S. Lim, J. H. Lee, A. Ikeda-Ohno, T. Ohkochi, K.-S. Kim, J. Seidel, C.-H. Yang, Electric-field-induced insulator to Coulomb glass transition via oxygen-vacancy migration in Ca-doped $BiFeO_3$. *Phys. Rev. B* **94**, 035123 (2016).
16. H.-B. Li, N. Lu, Q. Zhang, Y. Wang, D. Feng, T. Chen, S. Yang, Z. Duan, Z. Li, Y. Shi, W. Wang, W.-H. Wang, K. Jin, H. Liu, J. Ma, L. Gu, C. Nan, P. Yu, Electric-field control of ferromagnetism through oxygen ion gating. *Nat. Commun.* **8**, 2156 (2017).
17. A. Khare, D. Shin, T. S. Yoo, M. Kim, T. D. Kang, J. Lee, S. Roh, I.-H. Jung, J. Hwang, S. W. Kim, T. W. Noh, H. Ohta, W. S. Choi, Topotactic metal-insulator transition in epitaxial $SrFeO_x$ thin films. *Adv. Mater.* **29**, 1606566 (2017).
18. J. Tian, H. Wu, Z. Fan, Y. Zhang, S. J. Pennycook, D. Zheng, Z. Tan, H. Guo, P. Yu, X. Lu, G. Zhou, X. Gao, J.-M. Liu, Nanoscale topotactic phase transformation in $SrFeO_x$ epitaxial thin films for high-density resistive switching memory. *Adv. Mater.* **31**, 1903679 (2019).
19. V. R. Nallagatla, T. Heisig, C. Baeumer, V. Feyer, M. Jugovac, G. Zamborlini, C. M. Schneider, R. Waser, M. Kim, C. U. Jung, R. Dittmann, Topotactic phase transition driving memristive behavior. *Adv. Mater.* **31**, 1903391 (2019).
20. J. Berggren, Refinement of the crystal structure of dicalcium ferrite, $Ca_2Fe_2O_5$. *Acta Chem. Scand.* **25**, 3616–3624 (1971).
21. J. Young, J. M. Rondinelli, Crystal structure and electronic properties of bulk and thin film brownmillerite oxides. *Phys. Rev. B* **92**, 174111 (2015).
22. F. Kanamaru, H. Miyamoto, Y. Mimura, M. Koizumi, M. Shimada, S. Kume, S. Shin, Synthesis of a new perovskite $CaFeO_3$. *Mat. Res. Bull.* **5**, 257–261 (1970).
23. P. C. Rogge, R. U. Chandrasena, A. Cammarata, R. J. Green, P. Shafer, B. M. Lefler, A. Huon, A. Arab, E. Arenholz, H. N. Lee, T.-L. Lee, S. Nemšák, J. M. Rondinelli, A. X. Gray, S. J. May, Electronic structure of negative charge transfer $CaFeO_3$ across the metal-insulator transition. *Phys. Rev. Mater.* **2**, 015002 (2018).
24. O. A. Dicks, A. L. Shluger, P. V. Sushko, P. B. Littlewood, Spectroscopic properties of oxygen vacancies in $LaAlO_3$. *Phys. Rev. B* **93**, 134114 (2016).
25. J. S. Lim, J. H. Lee, H.-S. Park, R. Gao, T. Y. Koo, L. W. Martin, R. Ramesh, C.-H. Yang, Ultrafast collective oxygen-vacancy flow in Ca-doped $BiFeO_3$. *NPG Asia Mater.* **10**, 943–955 (2018).
26. H.-S. Park, J. S. Lim, J. Suh, C.-H. Yang, Real-time observation of filamentary conduction pathways in Ca-doped $BiFeO_3$. *Appl. Phys. Lett.* **115**, 183901 (2019).
27. J. Matsuno, T. Mizokawa, A. Fujimori, Y. Takeda, S. Kawasaki, M. Takano, Different routes to charge disproportionation in perovskite-type Fe oxides. *Phys. Rev. B* **66**, 193103 (2002).
28. O. Haas, U. F. Vogt, C. Soltmann, A. Braun, W.-S. Yoon, X. Q. Yang, T. Graule, The Fe K-edge X-ray absorption characteristics of $La_{1-x}Sr_xFeO_{3-\delta}$ prepared by solid state reaction. *Mater. Res. Bull.* **44**, 1397–1404 (2009).
29. S. Inoue, M. Kawai, N. Ichikawa, H. Kageyama, W. Paulus, Y. Shimakawa, Anisotropic oxygen diffusion at low temperature in perovskite-structure iron oxides. *Nat. Chem.* **2**, 213–217 (2010).
30. S. Yun, C.-S. Woo, G.-Y. Kim, P. Sharma, J. H. Lee, K. Chu, J. H. Song, S.-Y. Chung, J. Seidel, S.-Y. Choi, C.-H. Yang, Ferroelastic twin structures in epitaxial WO_3 thin films. *Appl. Phys. Lett.* **107**, 252904 (2015).
31. Y. Lin, S. Fang, D. Su, K. S. Brinkman, F. Chen, Enhancing grain boundary ionic conductivity in mixed ionic–electronic conductors. *Nat. Commun.* **6**, 6824 (2015).
32. H. Tan, Z. Zhao, W.-B. Zhu, E. N. Coker, B. Li, M. Zheng, W. Yu, H. Fan, Z. Sun, Oxygen vacancy enhanced photocatalytic activity of pervoskite $SrTiO_3$. *ACS Appl. Mater. Interfaces* **6**, 19184–19190 (2014).
33. D. Kan, T. Terashima, R. Kanda, A. Masuno, K. Tanaka, S. Chu, H. Kan, A. Ishizumi, Y. Kanemitsu, Y. Shimakawa, M. Takano, Blue-light emission at room temperature from Ar^+-irradiated $SrTiO_3$. *Nat. Mater.* **4**, 816–819 (2005).
34. M. W. Kim, P. Murugavel, S. Parashar, J. S. Lee, T. W. Noh, Origin of the 2 eV peak in optical absorption spectra of $LaMnO_3$: An explanation based on the orbitally degenerate Hubbard model. *New J. Phys.* **6**, 156 (2004).
35. X. S. Xu, T. V. Brinzari, S. Lee, Y. H. Chu, L. W. Martin, A. Kumar, S. Mcgill, R. C. Rai, R. Ramesh, V. Gopalan, S. W. Cheong, J. L. Musfeldt, Optical properties and magnetochromism in multiferroic $BiFeO_3$. *Phys. Rev. B* **79**, 134425 (2009).
36. S. Cong, Y. Tian, Q. Li, Z. Zhao, F. Geng, Single-crystalline tungsten oxide quantum dots for fast pseudocapacitor and electrochromic applications. *Adv. Mater.* **26**, 4260–4267 (2014).
37. S. Yoon, S.-H. Kang, S. Lee, K. Kim, J.-P. Song, M. Kim, Y.-K. Kwon, A "non-dynamical" way of describing room-temperature paramagnetic manganese oxide. *Phys. Chem. Chem. Phys.* **21**, 15932–15939 (2019).
38. M. Cococcioni, S. de Gironcoli, Linear response approach to the calculation of the effective interaction parameters in the LDA+U method. *Phys. Rev. B* **71**, 035105 (2005).
39. M. Fox, *Optical Properties of Solids* (Oxford Univ. Press, 2001).
40. G. Kresse, D. Joubert, From ultrasoft pseudopotentials to the projector augmented-wave method. *Phys. Rev. B* **59**, 1758 (1999).
41. H. Ullmann, N. Trofimenko, Estimation of effective ionic radii in highly defective perovskite-type oxides from experimental data. *J. Alloys Compd.* **316**, 153–158 (2001).
42. V. L. Deringer, A. L. Tchougréeff, R. Dronskowski, Crystal orbital Hamilton population (COHP) analysis as projected from plane-wave basis sets. *J. Phys. Chem. A* **115**, 5461–5466 (2011).

Acknowledgments

Funding: This work was supported by a National Research Foundation (NRF) of Korea Grant funded by the Korean Government through the Creative Research Center for Lattice Defectronics (grant no. NRF-2017R1A3B1023686) and the Center for Quantum Coherence in Condensed Matter (2016R1A5A1008184). J.L., H.-H.N., and Y.-H.K. were also supported by a NRF of Korea program (2018R1A2A2A14079326). **Author contributions:** J.S.L. and C.-H.Y. conceived and designed the project. J.S.L., H.-S.P., and J.S. prepared the samples and devices with basic characterizations and performed real-time electroforming processes with color tracing analyses. B.J.L. and E.C. carried out optical absorption measurements. J.L., H.-H.N., and Y.-H.K. performed first-principles DFT calculations. Y.-J.K., H.-S.P., J.S.L., S.-W.K., B.-G.C., and T.Y.K. performed x-ray diffraction for structural characterization. J.S.L., Y.-H.K., and C.-H.Y. led the manuscript preparation with contributions from all authors. **Competing interests:** The authors declare that they have no competing interests. **Data and materials availability:** All data needed to evaluate the conclusions in the paper are present in the paper and/or the Supplementary Materials. All electronic structure data contained in this work were generated with the VASP code (*40*). The code is available for a license fee from https://www.vasp.at.

Submitted 23 March 2020
Accepted 19 August 2020
Published 9 October 2020
10.1126/sciadv.abb8553

Citation: J. S. Lim, J. Lee, B. J. Lee, Y.-J. Kim, H.-S. Park, J. Suh, H.-H. Nahm, S.-W. Kim, B.-G. Cho, T. Y. Koo, E. Choi, Y.-H. Kim, C.-H. Yang, Harnessing the topotactic transition in oxide heterostructures for fast and high-efficiency electrochromic applications. *Sci. Adv.* **6**, eabb8553 (2020).

Harnessing the topotactic transition in oxide heterostructures for fast and high-efficiency electrochromic applications

Ji Soo Lim, Jounghee Lee, Byeoung Ju Lee, Yong-Jin Kim, Heung-Sik Park, Jeonghun Suh, Ho-Hyun Nahm, Sang-Woo Kim, Byeong-Gwan Cho, Tae Yeong Koo, Eunjip Choi, Yong-Hyun Kim and Chan-Ho Yang

Sci Adv **6** (41), eabb8553.
DOI: 10.1126/sciadv.abb8553